The origin of vibrational mode couplings in various secondary structural motifs of polypeptides

Andrew Moran* and Shaul Mukamel†‡

*Department of Chemistry, Northwestern University, 2145 Sheridan Road, Evanston, IL 60208-3113; and †Department of Chemistry, University of California, Irvine, CA 92697-2025

Edited by Ernest R. Davidson, University of Washington, Seattle, WA, and approved October 20, 2003 (received for review May 23, 2003)

Electrostatic (through-space) and covalent (through-bond) contributions to couplings involving the C═O and C—N vibrational stretching modes of the amide group in the α-helix and the parallel and antiparallel β-sheet structures of alanine polypeptides are analyzed. Coupling constants computed at the density functional theory level are compared with the transition dipole coupling model and the complete electrostatic interaction between transition densities. We find that the transition densities of C═O modes are localized, and the electrostatic mechanism then holds. In contrast, the C—N mode transition densities are delocalized, and covalent contributions to the coupling are significant.

Secondary structural characteristics of proteins may be studied by using IR active marker bands localized on either the peptide backbone or its side chains. The structurally sensitive and strongly IR active amide I (mostly C′═O stretch) and amide II (mostly C′—N and C′—N—H bend) modes of the protein backbone are most suitable for structure elucidation (1–4). Different secondary structural elements have traditionally been identified by using empirical rules relating frequencies of broad and unresolved bands with particular structural motifs (1, 2, 5). The most commonly encountered motifs include: α- and 3_{10}-helices, parallel and antiparallel β-sheets, and β- and γ-turns. Recent theoretical and technological advances have led to the development of multidimensional IR techniques that enhance peak resolution, making the extraction of more refined structural information a possibility (6–18). A reliable interpretation of these newly available features requires accurate parameterization schemes for anharmonic vibrational Hamiltonians (3, 19–24). High-level *ab initio* methods are too expensive for peptides larger than 10–15 units, especially when the Hamiltonian must be parameterized at many steps along a molecular dynamics trajectory (26–28). For this reason, recent studies of amide modes in large peptides have turned to approximations such as electrostatic coupling (1, 2, 5, 19, 25, 27, 29) or the use of maps based on *ab initio* calculations for smaller units (4, 24, 26, 30, 31) to compute coupling constants.

Vibrational mode coupling among localized vibrations originates from the correlation of electron density at one position in the molecule with a nuclear coordinate located elsewhere. In general, the interaction originates from both through-space (electrostatic) and through-bond covalent contributions. The latter were shown to be important for amide I modes in adjacent peptide units, making it necessary to calculate these coupling coefficients by using *ab initio* methods because electrostatic models fail (29, 30). An *ab initio* map of the amide I bilinear coupling constants for adjacent units as a function of the (ϕ, ψ) Ramachandran angles (30) has been useful for parameterizing Hamiltonians in recent studies of trialanine (4, 19) and antamanide (24). However, determining the relative contribution of the two mechanisms for nonadjacent units requires further analysis.

In this work, we analyze vibrational coupling mechanisms for C═O and C—N stretching modes between all pairs of local modes for the α-helix and both parallel and antiparallel β-pleated sheets of polyalanine. To that end we computed the bilinear coupling constants in the following three ways: (*i*) Direct analytical differentiation of density functional theory (DFT) energies; these inherently possess both through-space and through-bond contributions; (*ii*) the transition dipole coupling (TDC) model, which assumes electrostatic coupling of point dipoles; and (*iii*) complete electrostatic simulations using the transition density derivative distribution (TDDD). Comparing the three calculations allows to test the validity of the TDC and TDDD approximations. Our analysis is facilitated by examining contours of electron density gradients with respect to displacements in local modes plotted in real-space to reveal coherence sizes associated with local mode transition densities.

The TDC model was shown to fail in the case of adjacent neighbors (30). Higher-order multipoles must be included when the separation between units is comparable to the transition dipole length. This discrepancy can be easily corrected because transition densities may be calculated in real space. For example, derivatives of Mulliken charges located on amide atoms were used to compute coupling constants for amide I modes (19, 27, 29). The TDDD method treats real-space electrostatic interaction more rigorously by calculating the three-dimensional distribution of transition density derivatives.

The three methods used to compute coupling constants are described in *Coupling Constants Between Local Modes*. Application to the α-helix and parallel and antiparallel β-sheets are presented in *Application to Typical Structural Motifs of Tetraalanine*. In *Discussion*, our results are analyzed by using plots of transition density derivatives, and the implications of this study for vibrational Hamiltonian parameterization schemes are discussed.

Coupling Constants Between Local Modes

We introduce dimensionless local modes $\{Q_\alpha\}$ residing on the individual peptide units by rescaling the cartesian coordinates $\{Q'_\alpha\}$:

$$Q_\alpha = \left(\frac{M_\alpha \Omega_\alpha}{\hbar}\right)^{\frac{1}{2}} Q'_\alpha, \qquad [1]$$

where M_α is the reduced mass of mode α and Ω_α is the frequency. Using these dimensionless coordinates, we write the harmonic part of the vibrational Hamiltonian:

$$H = \frac{1}{2}\sum_\alpha \Omega_\alpha Q_\alpha^2 + \sum_{\alpha<\beta} J_{\alpha\beta} Q_\alpha Q_\beta. \qquad [2]$$

The bilinear coupling constant between local modes α and β ($J_{\alpha\beta}$) is the primary focus of this article.

This paper was submitted directly (Track II) to the PNAS office.

Abbreviations: DFT, density functional theory; TDC, transition dipole coupling; TDDD, transition density derivative distribution.

‡To whom correspondence should be addressed. E-mail: smukamel@uci.edu.

www.pnas.org/cgi/doi/10.1073/pnas.2533089100

All calculations were performed at the B3LYP/6–31+G(d,p) level by using GAUSSIAN 98 (32). In the DFT calculation (model *i*), $J_{\alpha\beta}$ was calculated by analytical differentiation of the potential energy to second-order with respect to modes α and β. Model *ii* (TDC) represents the transition density in a basis of multipolar transition moments by truncating the expansion at the leading dipole term, resulting in (2)

$$J_{\alpha\beta} = \frac{0.1}{\varepsilon}\frac{\delta\mu^{(\alpha)}\cdot\delta\mu^{(\beta)} - 3(\delta\mu^{(\alpha)}\cdot\mathbf{n}_{\alpha\beta})(\delta\mu^{(\beta)}\cdot\mathbf{n}_{\alpha\beta})}{R^{\beta}_{\alpha\beta}}, \qquad [3]$$

where $\delta\mu^{(\alpha)}$ is the transition dipole of mode α, $\mathbf{n}_{\alpha\beta}$ is a unit vector connecting the transition dipoles α and β, and ε is the dielectric constant. The TDC model was applied by computing dipole derivatives and taking the separation between dipoles ($R_{\alpha\beta}$ of Eq. **3**) to be the distance between the midpoints of either the C═O or C—N bonds. The TDC model is only valid when the separation between transition dipoles is much larger than the transition dipole length. Otherwise, higher-order multipoles must be taken into account. This calculation can be done by first expanding the charge density ρ with respect to the vibrational modes:

$$\rho(\mathbf{r}) = \rho^{(0)}(\mathbf{r}) + \sum_{\alpha}\left(\frac{\delta\rho(\mathbf{r})}{\delta Q_\alpha}\right)_0 Q_\alpha + \frac{1}{2}\sum_{\alpha\beta}\left(\frac{\delta^2\rho(\mathbf{r})}{\delta Q_\alpha \delta Q_\beta}\right)_0 Q_\alpha Q_\beta + \cdots \qquad [4]$$

The transition density with respect to mode α may then be computed by defining a volume element (A) and then calculating the electron density gradient with respect to a displacement in mode α at a collection of grid points i. The transition density at grid point i within A is represented by

$$M^A_{\alpha i}(\mathbf{r}_i) = \delta V_i \int_{\mathbf{r}_i}^{\mathbf{r}_i + \delta\mathbf{r}_i} d\mathbf{r}_i \left(\frac{\delta\rho(\mathbf{r}_i)}{\delta Q_\alpha}\right)_0. \qquad [5]$$

Electrostatic coupling between modes α and β is calculated by summing the coulombic interaction between their transition densities, which are confined to the nonoverlapping volume elements A and B, respectively. The coupling is then written as

$$J_{\alpha\beta} = \sum_{ij}\frac{M^A_{\alpha i}M^B_{\beta j}}{R_{ij}}, \qquad [6]$$

where R_{ij} is the separation between grid points and $J_{\alpha\beta}$ is defined by Eq. **2**. Eq. **6** may be used provided $\delta\rho/\delta Q_\alpha$ does not overlap spatially with $\delta\rho/\delta Q_\beta$, i.e., the charge gradient of mode α is very small in the region where it is large for mode β. We have taken the A and B spheres to be centered at the local modes. The model *iii* (TDDD) calculations were performed by using Eq. **6**. The midpoints of either the C═O or C—N bonds were taken to be the center of the transition density volumes (spheres denoted by A and B in Eq. **6**); the radii of the spheres are the same, so the sphere surfaces are in contact but do not overlap.

Application to Typical Structural Motifs of Tetraalanine

Coupling elements for α-helical tetraalanine computed by using the three levels of approximation outlined earlier are presented in Table 1. The TDC coupling constants are overestimated in all cases, especially for the C—N modes. The TDC couplings possess the same sign as the DFT energy derivatives for all but one of the C═O modes (J_{24}). However, the signs of the TDC couplings match the signs of the force constants for only one of the C—N modes (J_{23}). The TDDD parameters for the C═O modes are in better agreement with the DFT force constant calculations than for the C—N modes. In addition, the TDDD calculations are in better agreement with the DFT energy derivatives than the TDC parameters, which suggests that higher-order multipoles should be included at these interunit distances.

Table 1. Coupling elements computed by using different models for the α-helix

$J_{\alpha\beta}$*	DFT†	TDDD	TDC
		C═O modes	
J_{12}	6.92	6.13	54.71
J_{13}	−1.80	−3.08	−29.38
J_{14}	−5.56	−8.16	−66.94
J_{23}	6.29	10.51	45.88
J_{24}	−1.99	−1.15	15.72
J_{34}	6.91	15.16	75.85
		C—N modes	
J_{12}	1.04	60.66	−19.27
J_{13}	3.84	53.01	−15.58
J_{14}	5.67	50.63	−5.25
J_{23}	−1.67	55.37	−19.43
J_{24}	5.45	65.49	−14.50
J_{34}	3.23	44.02	−14.09

*The mode indices run from the nominal N to C termini (see Fig. 1). See Fig. 1 for mode indices. All parameters are reported in units of cm^{-1} corresponding to dimensionless local coordinates (Eq. **2**).

†These couplings are computed by using standard harmonic force constant output.

The coupling constants for the antiparallel β-sheet presented in Table 2 show trends similar to those found for the α-helix: the TDC couplings are overestimated in all cases, especially for the C—N modes, and the TDDD couplings are in reasonable agreement with the force constant calculation for the C═O modes but not the C—N modes. Also, the TDDD algorithm results in more accurate couplings than the TDC model, especially for the C═O modes.

Parameters calculated for the parallel β-sheet are presented in Table 3. The interunit coupling pattern for C═O modes of this motif is different from in the antiparallel case, where the strongest interunit couplings were between adjacent units on the same strand. Only the J_{13} DFT coupling is smaller in magnitude than those between adjacent units ($\approx$2 cm^{-1}). The TDDD model

Table 2. Coupling elements computed by using different models for the antiparallel β-sheet

$J_{\alpha\beta}$*	DFT†	TDDD	TDC
		C═O modes	
J_{12}	6.27	0.779	115.71
J_{13}	5.76	3.412	−94.32
J_{14}	−0.03	−0.255	−21.38
J_{23}	3.63	0.910	−18.15
J_{24}	−3.22	−1.251	−135.70
J_{34}	−11.53	1.584	162.88
		C—N modes	
J_{12}	2.63	23.309	−101.84
J_{13}	0.65	2.156	−36.41
J_{14}	0.39	−0.585	5.90
J_{23}	−0.28	1.248	−13.77
J_{24}	−1.80	−1.178	−16.74
J_{34}	−0.81	7.199	−68.51

*All parameters are reported in units of cm^{-1} corresponding to dimensionless local coordinates (Eq. **2**). See Fig. 2 for mode indices.

†These couplings are computed by using standard harmonic force constant output.

Table 3. Coupling elements computed by using different models for the parallel β-sheet

$J_{\alpha\beta}$*	DFT†	TDDD	TDC
	C═O modes		
J_{12}	1.56	8.86	24.05
J_{13}	0.70	1.68	41.80
J_{14}	−6.05	−3.74	−173.73
J_{23}	−4.20	17.10	−277.45
J_{24}	−9.28	−11.20	−71.95
J_{34}	−1.95	1.17	−73.57
	C—N modes		
J_{12}	−16.76	31.43	−33.40
J_{13}	0.02	38.61	1.23
J_{14}	−2.14	14.18	−3.13
J_{23}	−0.37	128.13	1.89
J_{24}	−4.97	25.84	−1.84
J_{34}	−4.20	138.59	−82.38

*All parameters are reported in units of cm^{-1} corresponding to dimensionless local coordinates (Eq. **2**). See Fig. 3 for mode indices.

†These couplings are computed by using standard harmonic force constant output.

provides a good description for nonadjacent C═O modes with the exception of the J_{23} constant, which is overestimated and carries the wrong sign. Again, the TDC couplings are inferior compared with TDDD.

Our results suggest that electrostatic coupling models are justified for C═O but not for C—N modes. The TDC model severely overestimates the couplings and fails in both cases. TDDD computations are in reasonable agreement with DFT energy derivatives for C═O modes in all three motifs but are inadequate for the couplings between C—N modes. These trends will be rationalized in the next section by examining the distributions of transition densities in real space.

Discussion

Contour plots of the transition densities are presented in Figs. 1–3. Modes amenable to electrostatic coupling approximations should reveal a TDDD surface only in the vicinity of the coordinate at sufficiently high contours. Delocalized transition densities are expected for modes possessing significant through-bond contributions to their couplings.

Fig. 1 shows electron density gradients (Eq. **5**) at several contours for the C═O and C—N modes in the α-helix. Displacements in the C═O mode result in a more localized perturbation of the electron density than for C—N; C—N displacements affect the electron density in the vicinity of all four oxygen atoms. The gradients of both C═O and C—N (unit 1) couple most strongly to their nearest neighbor (unit 2). The C—N gradients for different modes clearly overlap and therefore may not be used for electrostatic coupling calculations at these interunit distances. However, these calculations suggest that the electrostatic coupling approximation is reasonable for C═O modes.

Similar calculations for the antiparallel β-sheet are depicted in Fig. 2. The gradients with respect to the C═O mode are localized and are most strongly coupled to the adjacent neighbor on the same strand. The interunit C—N coupling are also most dominant between adjacent neighbors on the same strand. However, a displacement in the C—N mode (unit 2) results in a gradient delocalized over all four units. These plots further support the conclusion made for the α-helix, that electrostatic coupling is a reasonable approximation for C═O modes but not C—N modes.

Electron density gradients of the parallel β-sheet are presented in Fig. 3. The C═O gradient is highly localized and

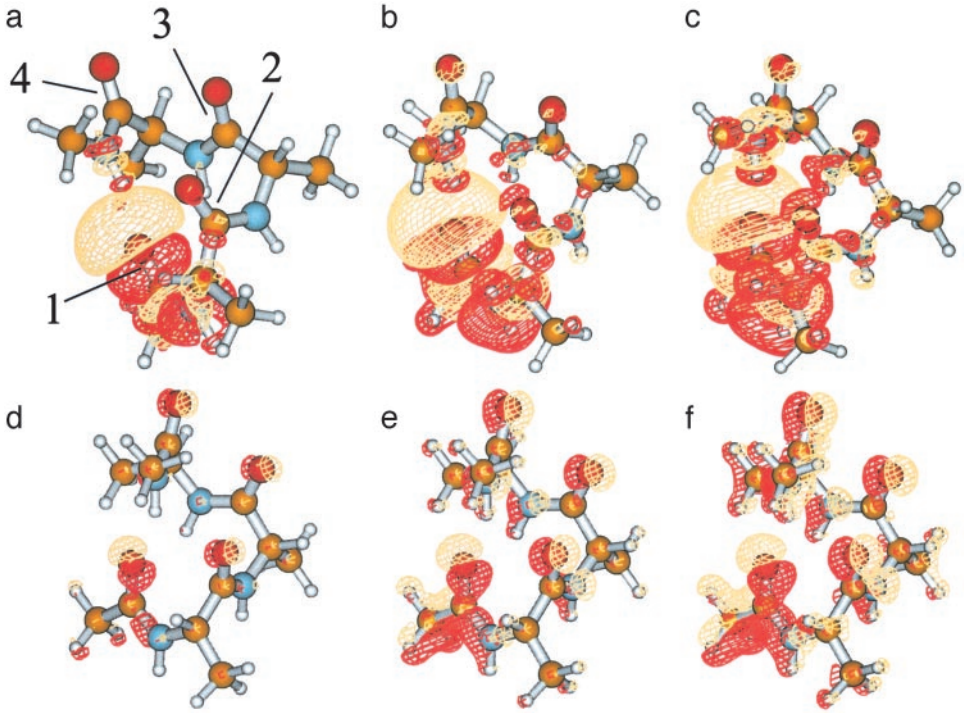

Fig. 1. Electron density gradient (Eq. **5**) with respect to the C═O mode of unit 1 (*a–c*) and the C—N mode of unit 1 (*d–f*) for the α-helix at various contours: 0.010 (*a*), 0.004 (*b*), 0.003 (*c*), 0.750 (*d*), 0.350 (*e*), and 0.250 (*f*) esu/bohr (1 esu/bohr = 6.303 C/m). Unit indices correspond to those given in Table 1. Red and beige contours represent positive and negative gradients, respectively. Atoms are labeled by color: oxygen (red), carbon (orange), nitrogen (blue), and hydrogen (white).

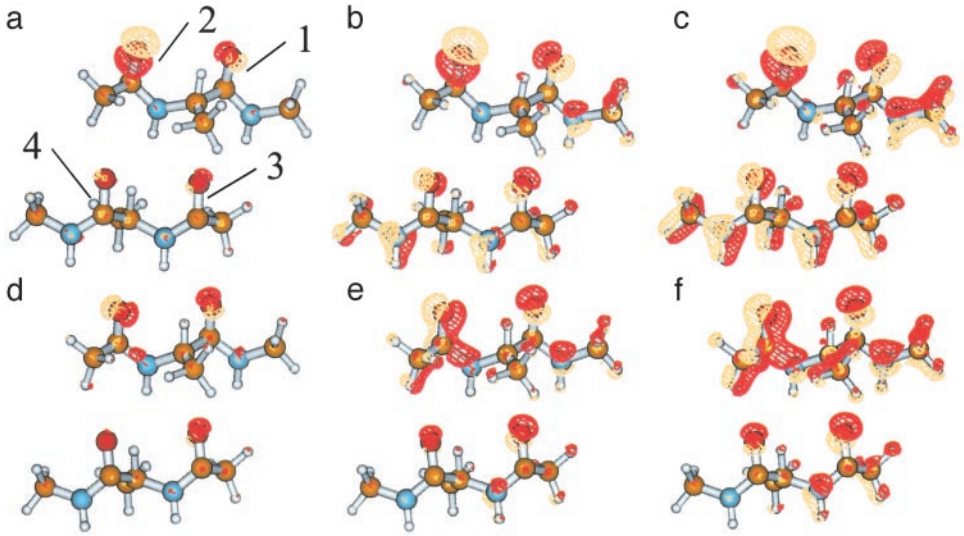

Fig. 2. Electron density gradient (Eq. **5**) with respect to the C═O mode of unit 2 (*a*–*c*) and the C—N mode of unit 2 (*d*–*f*) for the antiparallel β-sheet at the following contours: 0.300 (*a*), 0.150 (*b*), 0.125 (*c*), 1.100 (*d*), 0.650 (*e*), and 0.450 (*f*) esu/bohr. Unit indices correspond to those given in Table 2. Colors representing the contours and atoms are the same as in Fig. 1.

couples most strongly to neighbors on the different strand. In contrast to the C═O modes, the DFT C—N couplings are greatest in magnitude for modes on adjacent units. These C—N modes are evidently less sensitive to changes in the Ramachandran angles. Here, the C—N couplings are severely overestimated by using the TDDD model, although the TDC results are more reasonable than for all other motifs (with the exception of J_{34}).

Gradients with respect to C—N modes are delocalized to other units, making the inclusion of exchange interaction critical and negating the validity of coulombic coupling models. The origin of the difference between C═O and C—N gradients may be understood by considering the amide unit structure; the C═O bond points away from the peptide backbone, whereas the C—N bonds represent the most electron-dense locations on the backbone. The C—N mode transition densities can therefore interact through carbon–carbon bonds on the backbone (separated by two bonds). However, adjacent C═O modes are separated by three bonds and possess the most electron density on the atom farthest away from the backbone (oxygen). These conclusions are supported by the electron density gradient plots.

Knowledge of coupling mechanism origins is essential for developing tractable yet sufficiently accurate algorithms to parameterize vibrational Hamiltonians. Couplings between amide

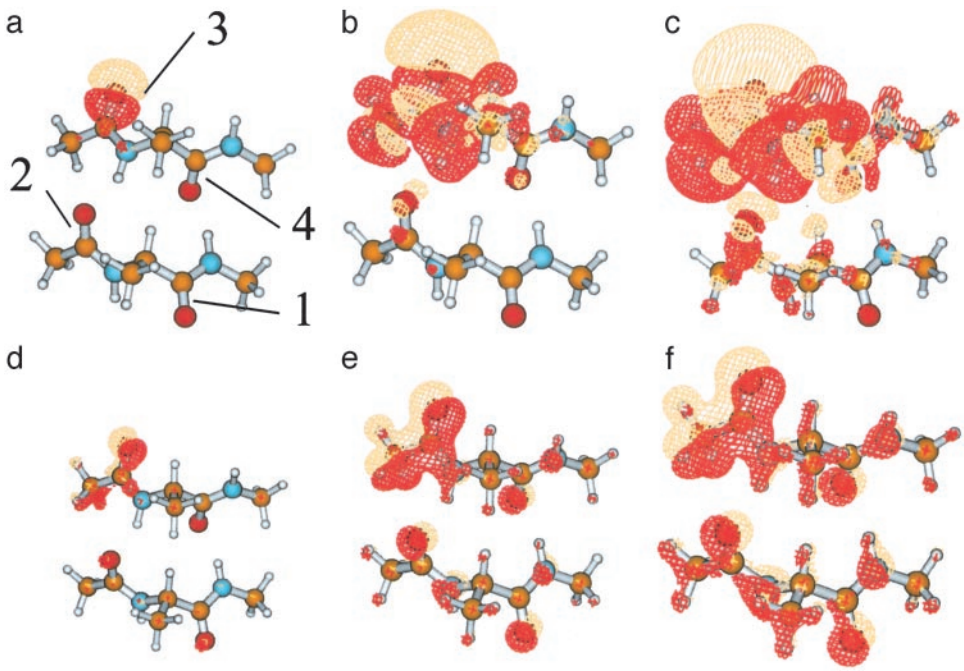

Fig. 3. Electron density gradient (Eq. **5**) with respect to the C═O mode of unit 3 (*a*–*c*) and the C—N mode of unit 3 (*d*–*f*) for the parallel β-sheet at the following contours: 0.075 (*a*), 0.003 (*b*), 0.001 (*c*), 0.700 (*d*), 0.200 (*e*), and 0.140 (*f*) esu/bohr. Unit indices correspond to those given in Table 3. Colors representing the contours and atoms are the same as in Fig. 1.

I modes (mostly C═O) may be computed by using electrostatic interaction models, although if high accuracy is needed then TDC should not be used for units that are as nearby as those considered here. TDC qualitatively captures the relative magnitude and signs of the couplings for C═O modes and their dependence on orientation, although the dipole derivatives should be empirically scaled (reduced) for adequate parameterization. Our simulations show that electrostatic interaction models are inadequate for C—N couplings at these interunit distances; a more elaborate parameterization scheme will be needed for interunit amide II couplings.

Accurate parameterization schemes are critical for experimental structure determination. To convert empirical parameters into a local amide mode basis, assumptions such as local mode transition dipole orientations and frequencies must be made because these states do not directly correspond to the measured spectra. Empirical couplings have thus far been based on calculations involving TDC (2, 5) or real-space calculations for Mulliken charge derivatives (27, 29). These models have given good agreement with experimental results for the α-helix ($J_{12} = 11.7\ cm^{-1}$, $J_{13} = -4.2\ cm^{-1}$, and $J_{14} = -7.6\ cm^{-1}$) (27) and are consistent with the calculations presented here. A model compound adopting the ideal β-sheet conformation has not yet been studied. However, Hamm and coworkers (4) found that trialanine exists in a conformation near this region of Ramachandran space ($\phi = -60°$, $\psi = 140°$) and possesses a J_{12} coupling of $6\ cm^{-1}$.

It is important to remember that our calculations were performed for isolated molecules and neglect solvation effects. The presence of a solvent should reduce the through-space couplings due to dielectric effects. However, the effect on through-bond interaction is more subtle, depending on both conformation and peptide constitution. An accurate description of through-bond interaction can be obtained by using QM/MM algorithms in which a lower level of theory (molecular mechanics) is applied to the solvent (33), whereas the solute is treated with DFT; this algorithm is favored over a continuum of descriptions because specific interactions such as hydrogen bonding are included.

This work was supported by National Institutes of Health Grant GM59230-01A2 and National Science Foundation Grant CHE-0132571.

1. Krimm, S. & Bandekar, J. (1986) *Adv. Protein Chem.* **38,** 181–364.
2. Torii, H. & Tasumi, M. (1996) in *Infrared Spectroscopy of Biomolecules*, ed. Mantsch, H. H. (Wiley-Liss, New York), pp. 1–18.
3. Zanni, M., Gnanakaran, S., Stenger, J. & Hochstrasser, R. (2001) *J. Phys. Chem. B* **105,** 6520–6535.
4. Woutersen, S. & Hamm, P. (2001) *J. Chem. Phys.* **114,** 2727–2737.
5. Torii, H. & Tasumi, M. (1992) *J. Chem. Phys.* **96,** 3379–3387.
6. S. Mukamel. (1995) *Principles of Nonlinear Optical Spectroscopy* (Oxford Univ. Press, New York).
7. Piratinski, A., Tretiak, S., Chernyak, V. & Mukamel, S. (2000) *J. Raman Spectrosc.* **31,** 125–135.
8. Mukamel, S. & Hochstrasser, R., eds. (2001) *Chem. Phys.* **266,** 135–351.
9. Tanimura, Y. & Mukamel, S. (1993) *J. Chem. Phys.* **99,** 9496–9511.
10. Laenen, R., Rauscher, C. & Laubreau, A. (1998) *Phys. Rev. Lett*. **80,** 2622–2625.
11. Laenen, R., Simeonidis, K. & Laubreau, A. (2002) *J. Phys. Chem. B* **106,** 408–417.
12. Stenger, D., Madsen, J., Dreyer, J., Hamm, P., Nibbering, E. & Elsaesser, T. (2002) *Chem. Phys. Lett*. **354,** 256–263.
13. Demirdoven, N., Khalil, M. & Tokmakoff, A. (2002) *Phys. Rev. Lett*. **89,** 237401.
14. Khalil, M., Demirdoven, N. & Tokmakoff, A. (2003) *Phys. Rev. Lett*. **90,** 047401.
15. Ge, N.-H., Zanni, M. & Hochstrasser, R. (2002) *J. Phys. Chem. A* **106,** 962–972.
16. Rubtsov, I., Wang, J. & Hochstrasser, R. (2003) *J. Phys. Chem. A* **107,** 3384–3396.
17. Gaffney, K., Piletic, I. & Fayer, M. (2003) *J. Chem. Phys*. **118,** 2270–2278.
18. Piletic, I., Gaffney, K. & Fayer, M. (2003) *J. Chem. Phys*. **119,** 423–434.
19. Woutersen, S. & Hamm, P. (2000) *J. Phys. Chem. B* **104,** 11316–11320.
20. Chaban, G., J. Jung, J. & Gerber, R. (1999) *J. Chem. Phys.* **111,** 1823–1829.
21. Gregurick, S., Chaban, G. & Gerber, R. (2002) *J. Phys. Chem. A* **106,** 8696–8707.
22. Moran, A. M., Dreyer, J. & Mukamel, S. (2003) *J. Chem. Phys*. **118,** 1347–1355.
23. Moran, A. M., Park, S.-M., Dreyer, J. & Mukamel, S. (2003) *J. Chem. Phys*. **118,** 3651–3659.
24. Moran, A. M., Park, S.-M. & Mukamel, S. (2003) *J. Chem. Phys*. **118,** 9971–9980.
25. Scheurer, C., Piryatinski, A. & Mukamel, S. (2001) *J. Am. Chem. Soc.* **123,** 3114–3124.
26. Woutersen, S., Mu, Y., Stock, G. & Hamm, P. (2001) *Proc. Natl. Acad. Sci. USA* **98,** 11254–11258.
27. Woutersen, S. & Hamm, P. (2001) *J. Chem. Phys.* **115,** 7737–7743.
28. Woutersen, S., Pfister, R., Mu, Y., Kosov, D. & Stock, G. (2002) *J. Chem. Phys*. **117,** 6833–6840.
29. Hamm, P., DeGrado, W. & Hochstrasser, R. (1999) *Proc. Natl. Acad. Sci. USA* **96,** 2036–2041.
30. Torii, H. & Tasumi, M. (1998) *J. Raman Spectrosc.* **29,** 81–86.
31. Choi, J.-H., Ham, S. & Cho, M. (2002) *J. Chem. Phys*. **117,** 6821–6832.
32. Frisch, M. J., Trucks, G. W., Schlegel, H. B., Scuseria, G. E., Robb, M. A., Cheeseman, J. R., Zakrzewski, V. G., Montgomery, J. A., Stratmann, R. E., Burant, J. C., *et al.* (1998) GAUSSIAN 98 (Gaussian, Pittsburgh), Revision A.9.
33. Vreven, T. & Morokuma, K. (1999) *J. Comp. Chem.* **21,** 1419–1432.